Journal Pre-proof

Characterization of Cebama –Low-pH Reference Concrete and assessment of its alteration with representative waters in Radioactive Waste Repositories

Tapio Vehmas, Vanessa Montoya, Maria Cruz Alonso, Radek Vašíček, Emily Rastrick, Stephane Gaboreau, Petr Večerník, Markku Leivo, Erika Holt, Nicolas Fink, Naila Ait Mouheb, Jiří Svoboda, David Read, Radek Červinka, Rita Vasconcelos, Claire Corkhill

PII: S0883-2927(20)30195-5

DOI: https://doi.org/10.1016/j.apgeochem.2020.104703

Reference: AG 104703

To appear in: *Applied Geochemistry*

Received Date: 4 July 2019

Revised Date: 20 July 2020

Accepted Date: 20 July 2020

Please cite this article as: Vehmas, T., Montoya, V., Alonso, M.C., Vašíček, R., Rastrick, E., Gaboreau, S., Večerník, P., Leivo, M., Holt, E., Fink, N., Mouheb, N.A., Svoboda, J., Read, D., Červinka, R., Vasconcelos, R., Corkhill, C., Characterization of Cebama –Low-pH Reference Concrete and assessment of its alteration with representative waters in Radioactive Waste Repositories, *Applied Geochemistry*, https://doi.org/10.1016/j.apgeochem.2020.104703.

Characterization of Cebama –Low-pH Reference Concrete and assessment of its alteration with representative waters in Radioactive Waste Repositories

Tapio Vehmas*[1], Vanessa Montoya*[2,9], Maria Cruz Alonso[3], Radek Vašíček[4], Emily Rastrick[5], Stephane Gaboreau[6], Petr Večerník[7], Markku Leivo[1], Erika Holt[1], Nicolas Fink[2], Naila Ait Mouheb[2], Jiří Svoboda[4], David Read[5], Radek Červinka[7], Rita Vasconcelos[8], Claire Corkhill[8]

[1]VTT Technical Research Centre of Finland, Espoo, Finland

[2] Institute for Nuclear Waste Disposal (INE), Karlsruhe Institute of Technology (KIT), 76021, Karlsruhe, Germany

[3] CSIC Institute of Construction Science Eduardo, Spain

[4] Faculty of Civil Engineering, Czech Technical University in Prague, Czech Republic

[5] University of Surrey, United Kingdom

[6] The French Geological Survey (BRGM), France

[7] ÚJV Řež, a. s., Czech Republic

[8] NucleUS Immobilisation Science Laboratory, Department of Materials Science and Engineering, University of Sheffield

[9]Department of Environmental Informatics – Helmholtz Centre for Environmental Research (UFZ), 04318, Leipzig, Germany

*tapio.vehmas@vtt.fi, VTT Technical Research Centre of Finland, Kemistintie 3, Espoo, P.O. Box 1000, FI-02044 VTT, Finland *vanessa.montoya@ufz.de, Department of Environmental Informatics – Helmholtz Centre for Environmental Research (UFZ), 04318, Leipzig, Germany

ABSTRACT

Concretes, mortars and grouts are used for structural and isolation purposes in radioactive and nuclear waste repositories. For example, concrete is used for deposition tunnel end plugs, engineered barriers, mortars for rock bolting and injection grouts for fissure sealing. Despite of the materials anticipated functionality, it is extremely important to understand the long-term material behaviour in repository environments. A reference concrete and mortar for the Cebama project based on a cement, silica and blast furnace slag ternary blend were designed and characterized in different laboratories with multiple experimental methods (XRD, XAS at the Fe and Cl K-edges, SEM-EDX, ^{29}Si and ^{27}Al MAS NMR, TG-DSC, MIP and Kerosene porosimetry) and techniques (punch strength tests). The reference concrete enabled comparison of results from different institutes and experimental techniques, unifying the individual results to more comprehensive body. The Cebama reference concrete and mortar were designed to have high durability and compatible formulation with respect to an engineered barrier system in clay or crystalline host-rocks, having pore solution pH significantly lower than traditional concretes. This work presents main results regarding their characterization and alteration in contact with representative waters present in radioactive waste repositories. Pore solution pH of the matured reference concrete was 11.4 - 11.6. The main hydrated phases were C-S-H and C-A-S-H gels with a Ca:Si ratio between 0.5- 0.7 and an Al:Si -ratio of 0.05. Minor phases were ettringite and hydrotalcite. Iron(III) could be in the C-S-H phases and no Cl-bearing solid phases were identified. Connected porosity and pore size distribution was characterized by MIP

observing that, as expected, the size of the pores in the hydrated cement phases varies from the micro- to the nanoscale. Connected porosity of both materials were low. Compressive strength of the concrete was 115 MPa, corresponding to traditional high-performance concrete. Degradation of these materials in contact with different waters mainly produce their decalcification and enrichment in Mg for waters containing high amount of this element, like the clay waters.

KEYWORDS: Low-pH cement, Blast furnace slag, Nuclear Waste Repository, Concrete, Mortar

1. INTRODUCTION

Nuclear power generation is a viable solution for decreasing CO_2 emissions and mitigating climate change at an intermediate time scale. However, a major disadvantage is production of nuclear waste in various forms and levels of radioactivity. The management and disposal of high-level waste (HLW) consisting of chemically processed and vitrified spent nuclear fuel or spent fuel itself will become a major task. Although the volume of HLW is small, compared to the total volume of nuclear waste generated, it contains 95% of the total radioactive inventory (World Nuclear Association, 2019).

Deep underground repositories are the most likely option for final disposal of HLW as well as for the Intermediate Level Long Lived Waste (IL-LLW). Depending on the selected site, final disposal concepts will vary to suit local conditions. However, all concepts must assure their long-term safety for periods ranging from tens of thousands to a million year, minimizing the release of radionuclides into the environment. According to current plans, the first HLW operational repositories will be in the Nordic countries and emplaced in crystalline bedrock (Posiva Oy, 2020). Clay-rock repositories are also a widely studied option, which will shortly follow crystalline-rock repositories (Nagra, 2019).

In deep underground repositories, HLW is disposed of in bedrock hundreds of metres below the surface, which naturally isolates the waste from the biosphere. The safety of the repository is ensured via a combination of natural and engineered barriers (see Figure 1). In the case of the KBS-3 disposal concept in crystalline rock (Moren, 2010), the engineered and geological barrier system comprises water- and gas-tight sealed copper canisters with a cast iron insert and the bentonite-based buffer, the backfill materials (Palomäki and Ristimäki, 2013) and the surrounding bedrock. Bentonite has an important role in many repository concepts, protecting the canister from small bedrock movements and potentially adsorbing any radionuclides released from the primary containment. Additionally, bentonite inhibits groundwater penetration into the repository and is intended to return the disposal environment to one close to natural conditions due to wetting-induced swelling (Palomäki and Ristimäki, 2013), Koskinen, 2014). On the other hand, concrete and other cementitious materials are used significantly in repositories for structural support and isolation purposes but also as engineered barrier, depending on the concept. For example, concrete plugs are used for sealing the repository and the deposition tunnels whilst also ensuring mechanical and hydrological isolation of various repository compartments (see Figure 1). In addition to concrete plugs, cementitious materials are used in shotcrete for tunnel wall rock supports, rock-bolting grouts and injection grouts for fissure sealing. However, independently, of their function, it is important that cementitious materials do not alter the engineered barrier system's performance within the long lifetime of the repository in order to meet safety requirements.

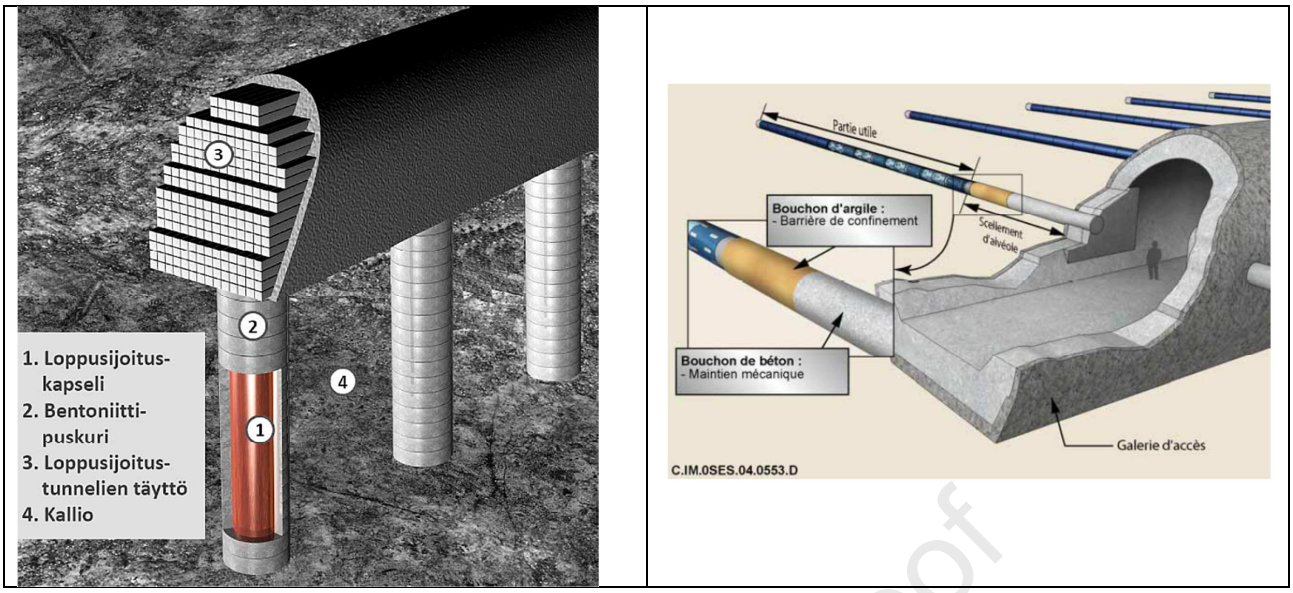

***Figure 1**. Left: multi-barrier system used in the KBS-3 concept. 1) Copper Canister, 2) Bentonite buffer 3) Bentonite backfill material 4) Bedrock (crystalline rock). Photo from the courtesy of Posiva Oy. Right: C-type waste (HLW) disposal cells of ANDRA (France), extracted from Dossier 2005 (ANDRA 2005).*

As indicated in Figure 1, groundwater or porewater, backfill/buffer and closure materials can be in direct contact with cementitious materials. Due to their different chemical properties, interactions between them will occur at the interfaces. These interactions could potentially involve changes in key properties of the buffer and host rock such as, geochemical composition, swelling pressure, hydraulic conductivity and pore structure. Migration of cementitious leachates may also affect the bentonite buffer, despite not being in direct contact with cementitious materials (Koskinen, 2014). For this reason, cementitious mix designs having suitable composition with respect to bentonite stability have been formulated (Bach, 2010; Cau Dit Coumes et al., 2006; Codina et al., 2008; Dole and Mattus, 2007; Garcia Calvo et al., 2010; Garcia et al., 2007; Holt et al., 2014; Lothenbach et al. 2008; Martino, 2007; Nishiuchi et al., 2007). These “low-pH” formulations consist of low alkaline Portland cements mixed with large amounts of supplementary pozzolanic materials (i.e silica fume or fly ash) and hydraulic materials (i.e. blast furnace slag), which hydrate themselves or react with the hydration products that control the pH and composition of cement pore solution. Consequently, these mix designs are still highly basic but the pH value is significantly lower than in traditional Portland cements. Mechanical properties and durability are usually considered to be similar to ordinary Portland cement-based formulations, although some disagreements still remain in terms of mechanical resistance against different waters attack (Dauzères et al., 2014).

Good examples of “low-pH” formulations are the successful casting and demonstration of massive tunnel end plugs, drifts and seals with ternary blended cements described in the DOPAS project (Holt et al., 2016), Noiret et al., 2012). In this case, the ”low-pH” concrete consisted of a ternary blend with low-alkali ordinary Portland cement, granulated silica fume and low-calcium fly ash. Although fly ash has been demonstrated to be a good option for “low-pH” mix designs (I.e. low water demand, relatively inexpensive material, high amorphous content), it also has drawbacks. For example, fly ash is a by-product of energy generation from combustion of fossil coal. As combustion of fossil coal is likely to be reduced over the next years, fly ash might not remain available throughout the construction and operational periods of a repository. Even if fly ash remains available throughout the repository construction period, it is expected that quality may decrease owing to the use of alternative fuel resources. The inhomogeneity of fly ash is already a problem, which will likely increase in the future (Taylor, 1997).

For the above reasons, new concrete designs are formulated and tested in order to fulfil the needed

112 requirements to be used in nuclear waste disposal. Slag-based "low-pH" mix designs has also recently
113 shown to have multiple benefits (Lothenbach et al., 2008, 2012a). Blast furnace slag is an industrial by-
114 product of iron and steel production with the advantage that it has substantially greater homogeneity than
115 fly ash due to production requirements. Due to the nature of its production, blast furnace slag is likely
116 available throughout the anticipated repository construction period. It is also a source of calcium but
117 without the excessive heat of traditional Portland cement, limiting temperature development in massive
118 structures.

119 In this work a new reference concrete and micro-mortar slag-based ternary mixes were designed and
120 characterized as potential material to be used in the context of nuclear waste disposal, which require high
121 durability during the extremely long times of disposal. Mechanical, chemical, microstructural and hydraulic
122 characterization were performed by eight laboratories of the Cebama (Cement-based materials, properties,
123 evolution, barrier functions) project consortium. The basis of the Cebama reference concrete was a ternary
124 mix design that has been used successfully in full scale demonstrations (Holt and Koho, 2016; Leivo et al.,
125 2014). The micro-mortar version was used to provide more detailed information on the binder phase and
126 can be considered as an aggregate-free concrete.

127 In addition, alteration and evolution with time of the designed concrete and micro-mortar in contact with
128 different representative waters in radioactive waste repositories (i.e. clay, crystalline, saline, bentonite)
129 have been studied by percolation, compressive punch test and leaching experiments.

130

131 **2. MATERIALS**

132 **2.1. Cebama reference concrete and micro-mortar**

133 The mix designs for the concrete and micro-mortar are presented in Table 1. Although materials used for
134 their design were the same (except the aggregates), it is clear that direct comparison between both
135 materials is not possible as the ratios between the different materials and water are very different. The
136 ordinary Portland cement (OPC) used was low-alkali, medium heat ordinary Portland cement LA MH CEM I
137 42.5 from Cementa Ab (Annläggninscement Degerhamn). Granulated silica fume (SF) and blast furnace slag
138 (BFS) were from Finnsementti Oy (Parmix silika and Masuunikuona KJ400). Elemental compositions of the
139 binder materials were determined by X-ray fluorescence (XRF) and are presented in Table 2. The
140 superplasticizer for achieving the target workability was a naphthalene sulfonate (Pantarhit LK FM from Ha-
141 Be Betonchemie GmbH. Alternatively, a similar naphthalene sulfonate superplastizer from DEN BRAVEN
142 Czech and Slovak a.s., was used for some of the compressive punch strength tests (see section 3). The
143 aggregate was a local granitic material of Finnish origin from Rudus Oy. The particle size distribution of
144 aggregates is presented in Table 1. Quartz filler was from Sibelco Nordic Oy (Nilsiä). A description of the
145 batching procedure and more details of the mix design and materials are available elsewhere (Vehmas et
146 al., 2017). The major components, calcium/silica -ratio, binder content and water/binder -ratio were the
147 same as those of the silica and fly ash based ternary blends described in the literature (Vehmas et al.,
148 2017). Samples were cured for 24 hours at room temperature and relative humidity of 100%. After 24
149 hours, samples were demoulded and cured submerged in water up to an age of 28 days.

150 ***Table 1.*** *Mix designs of studied "low-pH" concrete and micro-mortar.*

Materials	Concrete [kg/m^3]	Micro-mortar [kg/m^3]
CEM I 42.5	105	468
Silica fume	110	491
Blast furnace slag	65	290

Quartz filler*	116	517
Agregates:		
0-1 mm	168	-
1-8 mm	770	-
8-16 mm	532	-
16-32mm	396	-
Water (effective)	120	312
Superplasticizer	16.8	75
Water/binder -ratio	0.43	0.25

***Particle size distribution: (70% < 63 µm and 30% between 63- 250 µm)*

Table 2. *Oxide composition of the binder materials (wt. %)*

Binder	CaO	SiO_2	Al_2O_3	SO_3	MgO	Fe_2O_3	K_2O	Na_2O	CO_2[a]	TiO_2	MnO	SrO	ZrO_2
SF	1.46	93.1	1.44	0.47	0.88	0.91	1.73	-	*n.d.*	-	-	-	-
OPC	66.2	17.9	3.52	3.92	0.68	5.17	0.645	0.08	1.32	0.23	0.25	0.03	0.01
BFS	42.3	32.6	10.23	2.54	7.86	0.78	0.61	0.62	*n.d*	1.70	0.38	0.05	0.03

n.d. = not determined. [a]CO_2 obtained by thermogravimetric analysis

2.2. Representative water compositions in Nuclear Waste Disposal

Different groundwater and porewater compositions have been used in the leaching, compressive strength evolution measurements and percolation experiments (see section 3). Water compositions are presented in Table 3 and detailed information on the groundwater origin and compositions are provided in the following references. In short, granitic waters (Granitic I, Granitic II and Granitic III) represent the artificial Allard (Lagerblad and Trägårdh, 1994), Grimsel (Turrero et al., 2006) and a natural water occurring in the Josef underground laboratory (Czech Republic), respectively. Saline groundwater represented an artificial NASK water (Gascoyne, 2002; Lagerblad and Trägårdh, 1994). Clay I emulated a Callovo-Oxfordian clay formation pore water (Vinsot et al., 2008), Holt et al., 2016) and Clay II a Febex bentonite porewater (Turrero et al., 2006, 2011). The B75 water was prepared by using a bentonite B75 suspension and the Granitic water III (S:L ratio 1:5) (Večernik et al. 2016). Bentonite artificial porewater was prepared inside an argon (Ar) glove-box according to the water composition provided by (Bradbury and Baeyens, 2011) for a MX-80 bentonite.

Table 3. *Groundwater and porewater composition (mg/l), used in the methods described in the section 3.*

[mg/l]	*Granitic I*	*Granitic II*	*Granitic III*	*Saline*	*Clay I*	*Clay II*	*B75*	*Bentonite**
Na	*63.2*	*0.4*	*18.3*	*3035.9*	*1118.1*	*130.0*	*349.0*	*5773*
K	*4.1*	*0.0*	*2.0*	*104.7*	*52.6*	*0.7*	*13.0*	*73.6*
Mg	*4.7*	*0.0*	*15.4*	*8.2*	*153.7*	*8.9*	*3.9*	*230*
Ca	*16.2*	*0.2*	*76.1*	*682.3*	*241.4*	*11.0*	*5.0*	*596*
Sr	-	-	-	-	-	-	-	*9.1*
Al	-	-		-	-	-	-	*0.01200*
Fe	-	-		-	-	-	-	$0.8x10^{-3}$
Cl	*75.2*	*0.0*	*14.7*	*6246.9*	*1901.5*	*24.0*	*21.4*	*8271.5*
Br	-	-	-	-	-		-	-
SO_4	*7.4*	*0.1*	*106.2*	*470.1*	*1434.8*	*76.0*	*159.5*	*694.8*
Si	-	-	-	-	-	-	-	*2.1*
HCO_3^-	-	*0.4*	*199.6*	-	-	*3.2*	*604.1*	*12.3*

pH	*8.1*	*9.7*	*7.7*	*7.6*	*6.3*	*8.0*	*8.8*	*8.0*

**artificial porewater prepared inside an argon (Ar) glove-box according to the water composition provided by* (Bradbury and Baeyens, 2011)*. Different amounts of solids (20.18 g NaCl, 0.23 g KCl, 3.04 g $MgCl_2$ $6H_2O$, 0.857 g $MgSO_4$ $7H_2O$, 0.06 g $SrCl_2$ $6H_2O$, 0.094 g Na_2CO_3, 19.89 g Na_2SO_4, 4.11 g $CaCl_2$ $2H_2O$, 10.01 g $CaCO_3$) were dissolved in 2 L ultrapure water (MilliQ system, Millipore) in a PE bottle. Additionally, 60 µL of a solution of 6.16 M $Na_2O_7Si_3$ (water glass) and 16 mL of sulfuric acid H_2SO_4 (0.04 M) were added to adjust the silicon content and the pH of the solution, respectively.*

3. METHODS

3.1 Characterization of the micro-mortar

Workability was measured using the Haegermann method according to DIN 1164. Air content, compressive strength and density were determined according to standards (SFS-EN 12350-2, SFS-EN 12350-7, EN 12390-3 and EN12390-9). Additionally, the time evolution of the compressive strength was determined using a non-standard compressive punch test (Czech Geological Institute, 1987, Večernik et al., 2016, Vašiček et al. 2019) with thin cylindrical plates with high surface/ volume ratio (diameter, 50.0 mm and thickness, 8.2 mm). In short, the sample is located between two punches (diameter 7.98 mm with contact area of 50 mm2) and loaded until breakage while a force is applied (F, [N]). The press head displacement (related to deformation of the sample) is recorded. Verification of the punch method by comparison with the standard one described in ČSN EN 196-1 (using 40 mm cubes) was also performed. Various mortars with different uniaxial strength were tested by both methods to verify the relation of standard and non-standard tests. The value of uniaxial punch strength RP [MPa] was calculated as described in (Czech Geological Institute, 1987):

$$R_P = F^*/A \qquad \textit{(Equation 1.)}$$

where A is an ideal area (123 $mm^{2)}$ for punch of 7.98 mm and 50 mm diameter sample and a linear relationship was used to correlate the non-standard with the standard test results R_{cube} [MPa] (Večernik et al., 2016):

$$R_{cube} = R_P * 1.609 + 6.939 \qquad \textit{(Equation 2.)}$$

Punch test were performed using various groundwater compositions (Granitic III and B75 indicated in Table 3) and temperatures in order to evaluate groundwater influence on mechanical properties. The rigidity (or stiffness) [kN/mm] was derived from the linear section of force/ displacement relation of the particular strength test to have another indicator of potential changes of mechanical properties. Each punch test result consisted of 9-12 measurements according to available number of tested samples. Then the average value of each dataset was provided. Statistical evaluation (test for outliers and uncertainty calculation with confidence interval 95 %) was performed for each dataset. Expanded relative uncertainties of the sets were between 0.8 % and 8.2 % (only 3 datasets had an uncertainty above 5.3 %).

The chemical and structural properties were determined by using different complementary techniques. Initially, 5 mm of sample was removed from the surface to obtain regions unaffected by atmospheric carbon dioxide. For analysis by X-Ray Diffraction (XRD), thermogravimetric analysis / differential scanning calorimetry (TG-DSC) and ^{29}Si and ^{27}Al Magic Angle Spinning Nuclear Magnetic Resonance (^{29}Si and ^{27}Al MAS NMR), samples were crushed manually and powdered in an agate-ball grinder for only 2 minutes to avoid changes in the phase assemblage due to grinding (Scrivener et al. 2018). Ground samples were immersed in

isopropanol for 15 minutes, then filtered using a Buchner funnel. The samples were dried in a compartment dryer at 40°C for 10 min to ensure elimination of isopropanol. For X-ray absorption spectroscopic measurements, pellets were pressed after mixing powdered samples with boron nitride.

Scanning electron microscopy - energy dispersive X-ray spectroscopy (SEM-EDX) measurements were performed using an ESEM (model FEI Quanta 650 FEG), equipped with an EDX spectrometer (model Thermo Scientific NORAN System 7) for elemental microanalysis. XRD analysis was performed with a Bruker D8 ADVANCE diffractometer using Cu Kα radiation under controlled N_2 atmosphere using a low background and air-tight sample holder. TG-DSC was conducted using a heating rate of 10°C/min from 25 to 1200 °C with a STA409 (Netzsch Gerätebau GmbH) under N_2 atmosphere. The ^{29}Si and ^{27}Al MAS NMR spectra were acquired with Bruker Avance III 400 wide-bore spectrometer with a magnetic field strength of 9.4 T at 104.28 MHz for ^{27}Al and 79.50 MHz for ^{29}Si. Free induction decay was recorded with only 8k-16k data points. The observed ^{29}Si resonances were analysed using the $Q_n(mAl)$ classification (where Q refers to a Si tetrahedron connected to n Si tetrahedral with n varying from 0 to 4 and m indicating the number of neighbouring AlO_4 tetrahedra. (Engelhardt and Michel, 1987)

Additional information about the mineralogical composition was provided by X-ray absorption spectroscopy (XAS) at the Fe and Cl K-edges. XAS is complementary to the above mentioned techniques, it is element specific and does not suffer from overlapping signals from Al- and Fe-containing phases. Furthermore, the application of XAS does not require compounds to be crystalline. Fe K-edge XAS data were recorded at the BM26A beamline (Nikitenko et al., 2008) at the European Synchrotron Radiation Facility (ESRF, Grenoble, France). Fe K-edge spectra for powdered micro-mortar, concrete and reference compounds were recorded either in transmission or in fluorescence detection mode using a 9 element monolithic Ge fluorescence detector. Selected reference compounds are C2F ($Ca_2Fe_2O_5$), C4AF (Ca_2FeAlO_5), the starting clinker (LA MH CEM I 42.5 from Cementa Ab), hematite (α-Fe_2O_3), ferrihydrite, silica fume (Elkem, USA) (see Table 2 for iron content), C-S-H phases and ferric sulphate ($Fe_2(SO_4)_3.xH_2O$), Alfa Aesar).The Fe K-edge spectrum of goethite was recorded in transmission mode at the BM30 beamline(Proux et al., 2006) at the ESRF. At all stations, the energy of the incoming X-ray beam was calibrated by assigning the first inflection point of the transmission Fe K-edge X-ray absorption near-edge structure (XANES) recorded for a Fe foil to 7112.0 eV. Cl K-edge XAS data were recorded at the INE-Beamline (Rothe et al., 2012) at the KIT Synchrotron Light Source (Karlsruhe, Germany) in fluorescence detection mode using a silicon drift detector. At this edge, the energy of the incoming X-ray beam was calibrated by assigning the maximum of the absorption edge recorded for KCl to 2822.8 eV. Several chlorine reference compounds were used, and solid compounds were stored in an oven at 40°C for at least 12 hours before measurements. Solutions were also prepared: 0.5 mol/l NaCl and an artificial cement porewater or ACW (5.9 mmol/l Na^+, 3.8 mmol/l K^+, 3.6 mmol/l Ca^{2+}, 2.8 µmol/l CO_3^{2-}, 5.8 mmol/l SO_4^{2-} and 3.8 mmol/l Cl^-, pH = 11). XAS data were treated following standard procedures using the Athena interface to the Ifeffit software (Ravel and Newville, 2005).

The evolution of the hydration process was monitored via pH and chemical composition analysis as a function of hydration time. For the analysis of pore water pH and chemical composition, the *ex-situ* leaching method described by (Alonso et al., 2012) was used. This method consists on mixing a certain amount of cement powder with deionised CO_2-free water obtaining a liquid/solid ratio equals to 2.5 L kg^{-1}. After an equilibration time of two weeks, phase separation is achieved by centrifuging the samples. Then, the supernatant from each container is filtrated and the composition and pH is analysed.

3.2 Leaching studies with the micro-mortar

Leaching studies of micro-mortar with different waters were performed at room temperature (20°C) by using two slightly different set-ups. The age of the micro-mortar in these studies were more than 5 months. In the experimental set-up used to study the alteration of the micro-mortar with the Clay I (Callovo Oxfordian), Crystalline I and Saline -groundwaters (see Table 3), the micro-mortar sample was submerged

in the solution at a solid/liquid ratio of 1 at the age of 28 days. 200 cm^3 micro-mortar cylindrical blocks (dimensions: 6.6 cm diameter and 5.9 cm height) were submerged in 200 cm^3 synthetic water and not changed throughout the experiment. The pH of the aqueous phase was determined using a Thermo Fisher Scientific Orion^{TM} 9165BNWP Combination Sure-Flow pH electrode, calibrated to pH 10.01 and 13.00 with standard buffer solutions. The experiments were performed in triplicate. The alteration zone was characterised SEM-EDX. The experimental set-up used to study the alteration of the micro-mortar with bentonite water was performed to fully saturated samples. Cubic samples (10x 10 x 10 mm) were sealed with an epoxy resin, except for the exposed surface. The samples were submerged in 40 ml bentonite porewater (Table 3) for 6 months in a controlled argon atmosphere. After exposure, the micro-mortar samples were immersed in isopropanol to displace the water and stop further reactions. The alteration zone was characterised by cutting the sample parallel to the flow direction and identifying the chemical perturbation using SEM-EDX. Additionally, after 6 months, the bentonite water was analysed for its concentration of cations and anions by inductively coupled plasma optical emission spectrometry (ICP-OES), inductively coupled plasma mass spectrometry (ICP-MS) and ion chromatography (IC).

Finally leaching experiments at different temperatures (10°C and 95°C) with the Granitic III and bentonite B75 water were performed (Vašiček et al., 2019). Micro-mortar samples were sealed in plastic tubes and the pH evolution were measured according to the method described by.(Alonso et al., 2012). Similarly, to the previous described experiments, the alteration zone was characterised SEM-EDX

3.3 Characterization of the concrete

Slump, air content, compressive strength and density were measured according to standards (SFS-EN 12350-2, SFS-EN 12350-7, EN 12390-3 and EN12390-9).

The chemical composition and structural properties were determined after 5 and 15 months aging in a chamber at 100% RH and 20°C. The samples were prepared for characterisation immediately after removing from the curing chamber. XRD (Bruker XD8 advance X-ray diffractometer Cu radiation), thermogravimetry (STD Q600 V20.9 build 20, at a heating rate of 10ºC/min)/ differential thermal analysis (TG/DTA) and SEM-EDX (in polished samples, Hitachi S-4800 and Bruker 5030 EDX) were performed. XRD samples were completed on enriched powder samples in cement paste by removing the coarse aggregates. Firstly the coarse aggregates were removed, then the sample was drilled to smaller size and aggregates above 2 mm were removed in order to enrich the sample in cement paste; finally the samples were milled up to powder with particle sizes <80µm. For the SEM tests, polished samples were prepared after embedding in epoxy resin and coating with carbon for characterisation. In addition, information on iron and chlorine speciation was obtained in the same way described in section 3.1 for the micro-mortar and by probing their K-edge by XAS. Porosity was measured using the techniques described in section 3.5.

Pore solution pH and composition were determined according to Alonso et al., (2012). A piece of concrete was powder grounded without removing the aggregates, to a particle size of 80 µm. 10g were mixed with 10mL of deionised water. The suspension stirred for 5 min and then filtered with 0.45µm filter. The pH was measured with a pH electrode stable in the alkaline range of 12. The ion content was determined by ionic chromatography without any dilution or acidification of the system.

3.4 Percolation experiments with the concrete

The experimental set-up described in Garcia-Calvo et al. (2010) was used for the percolation experiments. A concrete slice of 5 cm diameter and 5 cm length was placed between two cylinders of methacrylate of the same diameter. These cylinders of methacrylate contain holes in the centre which are used for the entry

and exit of the injected water. The set of methacrylate and concrete was inserted in a rubber tube and this in turn in a methacrylate tube of about 15 cm of height and radius similar to the cylinders and the sample. The possible gaps between the methacrylate tube and the rubber were sealed with epoxy resin to ensure that water circulated only through the pore network of the concrete sample. A constant water pressure of 8 MPa, was maintained to percolate groundwaters through the concrete samples of 5x5cm. The age of the samples at the initial of percolation tests was 5 months. The percolated water composition and pH were monitored during the test, including the volume of the effluent flux to obtain the hydraulic conductivity. Additionally, at the end of each percolation test, the chemical, mineralogical and microstructural alterations in concrete were analysed at several distances from the groundwater inlet using XRD, TG/DTA and SEM.

3.5 Porosity and density measurements (concrete and micro-mortar)

Free water needs to be removed from cementitious binders prior to pore structure characterization. In the literature, different drying procedures were described to remove the free water, all of them having, in more or less extend, effects on the initial pore structure and phase evolution (Gallé, 2001; Zhang et al., 2019). For, this reason, prior to the mercury intrusion and kerosene porosimetry measurements, the concrete and the micro-mortar were heated under vacuum at 100°C for at least 36 hours and cooled under vacuum to ensure that all water left the pores, keeping in mind that this could slightly affect the studied materials.

Mercury intrusion porosimetry (MIP) - Intrusion and extrusion curves were obtained using Micromeritics Autopore IV 9500 volumetric set up on blocks of 2 cm^3 from atmospheric pressure up to $200x10^6$ Pa. Cumulative pore throat size distribution, up to the critical pore diameter, was calculated from the intrusion curve based on Washburn's law and a contact angle of 141.3° (Washburn, 1921) , assuming a cylindrical pore shape.

The bulk density or apparent dry density (ρ) of each sample was obtained before the first pressure step ($3x10^3$ Pa). The total intrusion porosity φ(MIP) or connected/accessible porosity was also estimated from the maximum intruded specific volume of mercury V (intr.max) [m^3/kg] and ρ, [kg/m^3] using the following Equation 3.

$$\varphi(MIP) = V(intr.max) \times \rho \qquad \text{(Equation 3.)}$$

Kerosene porosimetry - Total bulk porosity (connected (accessible) and not connected) and the apparent dry density were measured by the kerosene porosity method described in Gaboreau et al., (2011), which is based on the Archimedes' principle.

Calculated porosity- Porosity was also calculated from the measured grain density (ρ_{gr}) (helium pycnometry using a micromeretics accupyc 2020) and the apparent dry density (ρ) (obtained by mercury intrusion porosimetry) according to the following Equation 4.

$$\varphi = 1 - (\rho/\rho_{gr}) \qquad \text{(Equation 4.)}$$

4. RESULTS AND DISCUSSION

4.1 Fresh-stage properties

Fresh stage properties of the concrete and the micro-mortar were measured after batching. The slump of the concrete was 180 mm, corresponding to typical easily workable concrete. The Haegermann flow of the

micro-mortar was 200 mm, indicating easy-to-use mortar without risk of segregation. The fresh density of the concrete was 2420 kg/m^3 and 2110 kg/m^3 for the micro-mortar. The measured air content for the concrete was 1.0%.

4.2 Mechanical properties

The compressive strength evolution of concrete and micro-mortar are presented in Table 4 by using both standard and non-standard punch test. At the age of 7 days, the compressive strength of the concrete was 47 MPa and 64 MPa for the micro-mortar. The compressive strength of the concrete was similar to high performance concrete yet the result for micro-mortar was higher than that of the concrete studied. The results on SFS-EN concrete (Table 4) show continuing, significant increase in strength between 424 and 728 days (of about 30 %). This continuous evolution of the mechanical properties over 728 days (~2 years) highlight the low kinetics of hydration of the studied materials and the impossibility to reach final properties within only 28 days. The study on the interaction of micro-mortar thin samples (Table 4, referred to punch test) under various conditions (granitic/ humid air, B75 water and temperature 10 or 95 °C) shows significant hardening during the initial phase of 9 months, with indication of stabilisation during a further 9 months. The non-standard punch test method, applied only to the micro-mortar and performed at 10°C, presented similar compressive strength values to the one measured with the standard method. In addition, the use of different waters did not have a big influence in the test results. Only, the bentonitic water (B75) slightly affected the rigidity (force-deformation, [kN/mm]) (Table 5). Bentonite suspension stabilised the rigidity value slightly below the level of initial tests while the reference and non-bentonite environment allowed a slow increase of rigidity during the testing period.

On the other hand the compressive strength of the micro-mortar was clearly dependent on the superplasticizer used (Table 5). Keeping in mind that all the superplasticizers used in this work were naphtalene based superplasticizers. The superplasticizer had a central role in dispersing cement and supplementary cementitious materials to ensure good reactivity. High dispersion of fines also increased workability and enabled good consolidation during sample manufacture. As observed in Table 5, a change in superplasticizer brand reduced compressive strength, and even a change in the plasticizer batch had also an effect on the micro-mortar compressive strength. There is no clear explanation for this effect, especially when only the different batch of the same superplasticiser was used. Some effect could be related to the time and storage conditions of the superplasticisers before use or minor time variations in preparation procedure and varying amount of mortar in the batches. At least two series of tests were performed for each punch test and the results show the same systematic results confirming this was not an error in the measurement. Therefore, even a small change in superplasticizer quality induced changes in compressive strength. Moreover, the plasticizer dosages used in this work greatly exceeded the manufacturer's recommendations, which likely caused or increased the effects observed

Table 4. *Compressive strength and densities of the concrete and the micro-mortar.*

Sample:	***Concrete***		***Micro-mortar***						
Method:	***SFS-EN***		***SFS-EN***		***Punch test***				
Environment:	***20^{o}C RH100%***		***20^{o}C RH100%***		***Humid air, 10^{o}C***	***Granitic III, 10^{o}C***	***B75, 10^{o}C***	***Granitic III, 95^{o}C***	***B75, 95^{o}C***
Age [d]	***Compressive strength [MPa]***	***Density [kg/m^3]***	***Compressive strength [MPa]***	***Density [kg/m^3]***	***Compressive strength [MPa]***				
7	*47*	*2420*	*64*	*2110*	-	-	-	-	-

14	-	-	-	-	*67*	-	-	-	-
28	*80*	*2430*	*104*	*2150*	*76*	-	-	-	-
64	-	-	-	-	*82*	-	-	-	-
275	-	-	-	-	*113*	*132*	*122*	*146*	*132*
424	*89*	*2420*	-	-	-	-	-	-	-
550	-	-	-	-	*112*	*116*	*109*	*146*	*129*
723	-	-	*149*	*2140*	-	-	-	-	-
728	*116*	*2450*	-	-	-	-	-	-	-

383

384 ***Table 5.*** *Rigidity values obtained with the punch test*

	Punch test				
	Humid air, 10°C	***Granitic III, 10°C***	***B75, 10°C***	***Granitic III, 95°C***	***B75, 95°C***
Age [d]	***Rigidity [kN/mm]***				
0	-	*31 ± 1*	-	-	-
275	*35 ± 1*	*32 ± 1*	*28 ± 3*	*33 ± 2*	*26 ± 4*
550	*40 ± 4*	*38 ± 2*	*28 ± 6*	*36 ± 4*	*30 ± 12*

385

386 ***Table 6.*** *The effect of superplasticizer quality to compressive strength in punch test*

	Punch test		
	Naphthalene *(Pantarhit)*	***Naphthalene*** *(Pantarhit)* ***Different batch***	***Naphtalene (****DEN BRAVEN)*
Age [d]	*Compressive strength [MPa]*		
7	-	*59*	*38*
14	*75*	*67*	*48*
28	*86*	*76*	*63*
42	*92*	-	*70*
49	*101*	*83*	-
56	-	-	*78*
63	*103*	*81*	*75*

387

388 *4.3 Microstructure, petrophysical properties (porosity and density)*

389 Microstructural characterisation by SEM indicated dense C-S-H phases and low permeability structure for
390 both the concrete and micro-mortar samples. Additionally, a good aggregate-cement paste of interfacial
391 transition zone (ITZ) for the concrete was observed. Non-reacted silica fume (with a characteristic spherical
392 shape), quartz and feldspar were also observed with the same technique.

393 Total and connected porosity was determined by applying the kerosene and mercury intrusion porosimetry
394 methods, respectively (Table 7). In addition, porosity was calculated by using the grain density obtained by
395 a helium pycnometer. Calculated porosities were 24.3 and 12.8 % for the micro-mortar and the concrete,
396 respectively in agreement with the measured total porosity by the kerosene method. However, mercury
397 intrusion porosity for both, the micro-mortar and the concrete was much lower, 6.1%, and between 2.3-
398 2.5%, respectively (Table 7). This means that most of the connected pores (connected porosity) in both
399 materials have pore-throat sizes below 7nm because mercury cannot penetrate these small pore-throats
400 [v]. Indeed, the mean pore size measured with mercury intrusion porosimetry was < 15 nm (Leroy et al.
401 2019) indicating that most of the connected porosity available for transport was nano-size, and the

structure of concrete and micro- mortar was dense. Although some small changes could occur during the drying process of the samples, prior to the porosity measurement, the general observations are still valid (Zhang et al., 2019).

***Table 7**. Porosities of the concrete and the micro-mortar.*

Material	**MIP**		**He pycno.**	**Kerosene porosity**		**Calculated porosity**
	Bulk density (ρ) (g/cm^3)	**Porosity, $\varphi_{МИП,}$ (%)**	**Grain density ρ_{gr}**	**Bulk density (ρ) (g/cm^3)**	**Porosity, φ_{KEP}(%)**	**φ = 1-(ρ/ρ_{gr}) (%)**
Micro-mortar	*1.88*	*6.1*	*2.48*	*1.83*	*26.2*	*24.3*
Concrete	*2.28*	*2.3*-2,5***	*2.61*	*2.28*	*12.5*	*12.8*

**measured after 5 months ** measured after 15 months.*

4.4 Chemical properties

Pore solution pH evolution for concrete and micro-mortar decreased over time due to proceeding pozzolanic reaction and C-S-H polymerization (see Table 8). The decrease of the Ca:Si ratio of the C-S-H phases has a large impact on the observed pH decrease in agreement with thermodynamic calculations (Idiart et al., 2020). For both materials, the pH is below than a portlandite saturated solution (pH 12.5) indicating that portlandite is not present in the system in accordance with the chemical composition expected regarding the mix formulation.

Elemental composition of concrete pore solution evolution with time was also determined and it is presented in Table 9. As can be observed, Al concentration decreases to very low concentrations (~$4x10^{-7}$ mol/l) due to the precipitation of Al- bearing phases (C-A-S-H and ettringite) which have been observed in the characterization of the solid. The same was observed for iron, in that case the precipitation of Fe-bearing phases restricted the iron concentrations to values below < $2x10^{-6}$ mol/l. Silicon concentrations in the aqueous solution remained at $1x10^{-3}$ mol/l and calcium concentration decreased slightly with time from $1x10^{-3}$ to $5x10^{-4}$ mol/l, mainly due to the formation of C-S-H phases with different Ca:Si -ratios. Magnesium remained low (< 10^{-5} mol/l) and was probably controlled by the presence and solubility of hydrotalcite and brucite at the studied times (Roosz et al. 2018, Bernard, 2017a, 2017b). Alkalis (Na and K) kept practically constant to concentrations of $4x10^{-3}$ and $1x10^{-4}$, respectively. In turn, sulphate concentration remained below $3x10^{-3}$ mol/l, controlled by ettringite solubility.

***Table 8.** pH evolution of studied concrete and micro-mortar (temperature = 20°C)*

	Concrete	**Micro-mortar**
Age (days)	***pH***	
7	*12.16*	-
19	*11.94*	-
28	*11.91*	*12.26*
150	*11.47*	*11.70*
424	*11.46*	*11.56*
728	*11.35*	*11.61*

***Table 9.** Elemental composition of concrete pore solution after 150 and 450 days.*

Water soluble ions [mg/l]	**Concrete (150 d)**	**Concrete (450 d)**
Al	*0.70*	*0.01*

Ca	*50.87*	*20.82*
Fe	*0.14*	*0.00**
Mg	*0.58*	*1.45*
S	*111.19*	*90.20*
Si	*50.53*	*40.75*
Na	*101.17*	*115.25*
K	*52.01*	*39.93*

**Under detection limit.*

Full characterization of the micro-mortar was possible by using different complementary analytical techniques (XRD, TG-DSC, SEM-EDX, ^{29}Si and ^{27}Al MAS NMR, XAS), even identifying solid solutions like Cl- and Fe- bearing phases (which are normally present as minor phases in the hydrates). The same was true for the concrete, but in that case ^{29}Si and ^{27}Al MAS NMR were not applied. Specifically, the XAS studies were applied to identify in situ Fe- and Cl-containing phases present in these complex materials, which is novel for the studied compounds. Fe can substitute Al in various phases, thereby forming solid solutions which are difficult to be determined with other standard techniques. XAS has already been shown to be a good complementary technique providing molecular-level information for classical cements (Dilnesa et al., 2014, Vespa et al. 2015), but till the present moment, this technique has never been applied for the same purposes in low pH cementitious materials. Solid solutions properties differ significantly from the ones of pure components which could clearly influence the capability of retaining radionuclides by the low pH cementitious materials studied here (Bruno and Montoya, 2012; Dilnesa et al., 2014).

Identified assemblage phases for the concrete and the micro-mortar are summarized in Table 10. Quartz, feldspar, biotite and muscovite were identified by XRD as the main crystalline phase present as aggregates and quartz filler in the case of the concrete, as shown in Figure 3 left. C-S-H phases and other hydrates were more complicated to be identified with this technique due to their amorphous nature and the overlap of peaks, but C-S-H phases could be observed as broad bands. The XRD of the micro-mortar (no shown), presented very broad peaks, but calcite, quartz and unreacted alite and belite were able to be identified in agreement with the work of Vasconcelos et al. (2020). Calcium-silicate-hydrates (C-S-H) and calcium-aluminate-silicate-hydrates (C-A-S-H) were clearly identified with ^{29}Si and ^{27}Al MAS in the micro-mortar. Furthermore, ettringite was identified in both materials as a minor phase with the same techniques, although a slightly decomposition of ettringite could have happened due to sample preparation (see section 3.1). TG-DTA of both materials presented a mass loss around 100-300°C which was attributed to C-S-H phases and ettringite (Scrivener et al., 2018), as shown in Figure 3 for concrete after aging of 5 months and 15 months. However, in this temperature range the mass loss can also be attributed to water bound to mineral surfaces, making a quantification of the C-S-H phases difficult (Schöler et al., 2015). The water bound by the micro-mortar (11%) was calculated according to the method described in (Schöler et al. 2015). The weight loss at 450 °C, indicative for portlandite was not observed, neither in micro-mortar nor in the concrete, in agreement with the measured pH (see Table 8). Additionally, the Ca/Si –ratio measured by SEM-EDX of the C-S-H phases were between 0.5-0.7 for both the concrete and the micro-mortar, with the Al/Si-ratio around 0.05. The ^{29}Si MAS NMR spectrum is depicted in Figure 4. A broad signal in the chemical shift range between -75 and -100 ppm was the main signal of the spectrum and was assigned to the Si present in the C-(A)-S-H phases. The overlap of the signals did not allow unambiguous deconvolution but it is know that the spectra of C-S-H phases consists of at least three resonances called Q1, Q2(1Al) and Q2 (Lothenbach et al., 2012a; Richardson, 1999, Vasconcelos et al. 2020). The main signal can also be overlapped with a minor signal of feldspar (-95 to -100 ppm). The signal at -69 ppm resulted from unreacted clinker (alite and belite). The broad feature at −110 ppm is characteristic of unreacted silica fume and quartz filler.

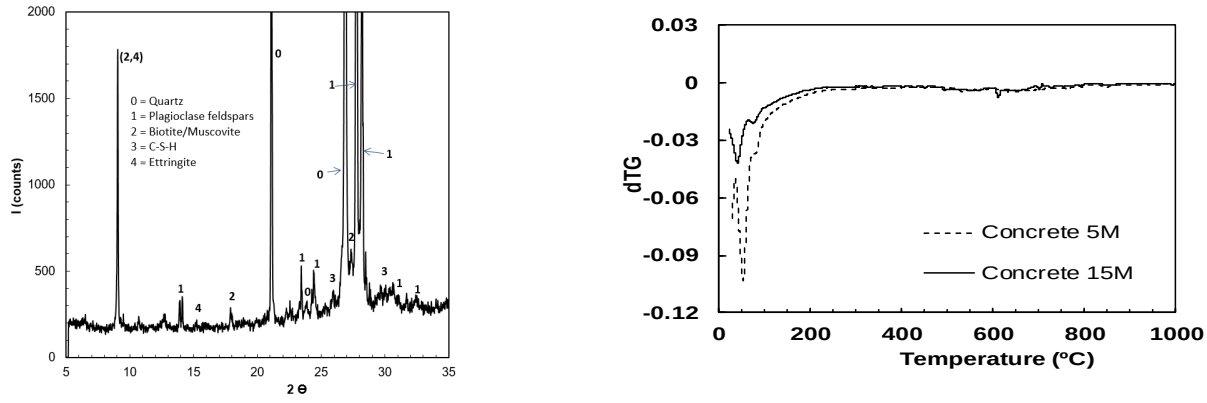

Figure 3: *X-ray diffractions (left) and differential thermogravimetric curves (right) for studied concrete*

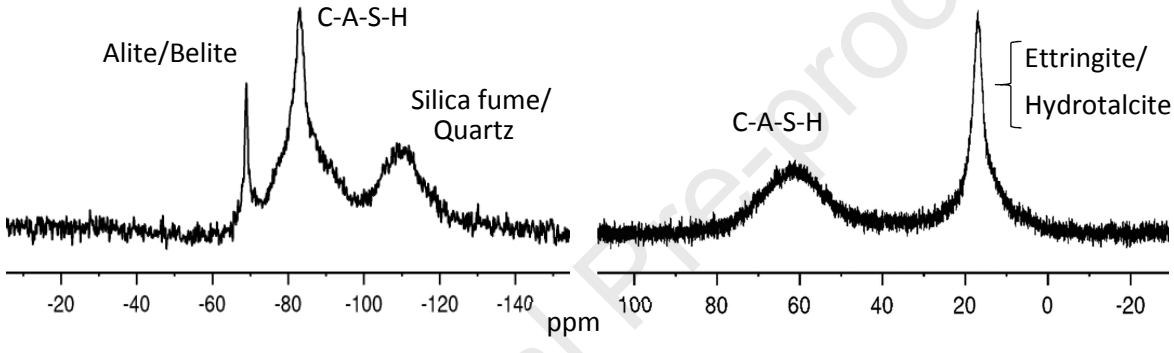

Figure 4: *^{29}Si MAS NMR spectra (left) and ^{27}Al MAS NMR spectra of the micro-mortar (right) in ppm.*

The ^{27}Al-MAS-NMR spectrum (Figure 4) presented two different signals at 63.0 and 16.7 ppm, indicating that Al was in both octahedral and tetrahedral coordination (L'Hôpital et al., 2016). The observed tetrahedrally coordinated ^{27}Al resonances were associated with the aluminium in the bridging position of the C-S-H phases and feldspar, and the octahedral ^{27}Al with the presence of ettringite and probably hydrotalcite-like phases (Walkley and Provis, 2019).

Information on Fe speciation in both materials was studied by probing the Fe K-edge by XAS. The XANES is particularly sensitive to the type and number of neighbouring elements as well as bond distances and geometrical arrangement. For all samples and reference compounds, the XANES exhibited a feature at around 7114.5 eV (Figure 5) that derived predominantly from $1s \rightarrow 3d$ transitions. In O_h symmetry, this transition is forbidden, whereas in T_d symmetry the $1s(a_1) \rightarrow t_2$ transition is allowed (Westre et al., 1997). Thus, no pre-edge feature should be observed for octahedrally coordinated Fe. However, very weak features were still observed, and the intensity depended on the local symmetry and electronic properties of the cation. The intensity of the pre-edge was therefore low for common octahedral sites (e.g., hematite, goethite) and substantial for tetrahedral sites. The pre-edge of the micro-mortar and the concrete were located at a position similar to reference compounds, which contained only ferric iron. Therefore, the micro-mortar and the cement contain Fe(III). Furthermore, the intensity of the pre-edge of the micro-mortar seemed slightly larger as in the concrete, implying that the former contained substantial amounts of tetrahedral Fe^{3+}, but the latter only marginal amounts.

Further information was obtained from the analysis of the main absorption edge. The XANES of the reference compounds C2F and C4AF were very similar with the presence of two shoulders (~7137 and ~7145 eV) on the high-energy side of the main absorption edge. This finding can be explained by the crystallization of both compounds in the same crystal system (orthorhombic). The XANES of the clinker also

bore similarities with that of C2F and C4AF, pointing to the presence of these compounds or at least one of them in the clinker. This finding compares well with reported data showing that the Fe-containing phases in the starting CEM I clinker are C2F and C4AF. Similarly, the XANES of both C-S-H phases (doped with Fe(III)) bore similarities, only the intensity of the shoulder after the main absorption edge slightly differed. The XANES of the micro-mortar differed from the concrete, implying the location of Fe in different chemical environments. The XANES of the former contained a shoulder, at ~7137 eV and weak feature at ~7145eV, whereas the XANES of the second is rather sharp and does not exhibit any significant feature. These findings may suggest the presence of ferrite C2F and/or C4AF and possibly C-(F)-S-H phases in the micro-mortar, and the absence of these phases in the concrete. Note that the XANES of C-(F)-S-H phases bear similarities with the reported XANES of siliceous hydrogarnet (Dilnesa et al. 2014), suggesting that this phase may actually be present in the micro-mortar. This finding would imply that the investigated micro-mortar and traditional ordinary Portland cement contain the same thermodynamically stable Fe-containing phases. For the micro-mortar these results also agreed with the observed intensity of the respective pre-edge features. The presence of minor amounts of other compounds was impossible to exclude. The XANES of the concrete significantly differed from that of most reference compounds. Though the XANES of ferrihydrite did not contained any shoulder, it differed from that of the concrete, which did not exclude the presence of low amounts of this reference compound in the sample.

Extended X-ray absorption fine structure (EXAFS) spectra of C2F and C4AF were very similar and observed differences in terms of oscillation amplitudes, was attributed to replacement of a fraction of Fe by Al within the structure (Figure 5). Though noisier, the spectrum of the clinker also was similar to that of these reference compounds. Likewise, the spectra of the C-(F)-S-H phases had similarities, suggesting closely related binding environments. These findings agree with analysis of the XANES. Other important information was derived from comparison of the spectra. The spectra of C2F, C4AF and the clinker had a first oscillation around 4.1 $Å^{-1}$, like most reference compounds, and a second oscillation or shoulder at ~4.8 $Å^{-1}$(Colville and Geller, 1971). Recently reported EXAFS spectra for ferric saponite, a smectite containing Fe^{3+} at tetrahedral position, exhibit oscillat (Finck et al., 2019), thus strengthening the attribution of this spectral feature to tetrahedral ferric iron. The EXAFS spectrum of the micro-mortar mainly differed from that of the concrete in the spectral features in the 4 – 6 $Å^{-1}$ range. Still, both had an oscillation amplitude maximum at ~4.1 $Å^{-1}$, implying the presence of octahedral Fe^{3+}. The spectrum of the micro-mortar had a shoulder at ~4.7 $Å^{-1}$ which was absent in the spectrum of the cement, whereas the spectrum of the cement had a feature at ~5.2 $Å^{-1}$ which was absent in the spectrum of the micro-mortar. By comparison with reference compounds, only spectra of C2F, C4AF and the clinker had a shoulder at k ~4.8 $Å^{-1}$, signifying that at least a fraction of Fe in the micro-mortar was located in an environment similar to that of these reference compounds. Interestingly, this result also agreed with the shoulder at k ~7 $Å^{-1}$ in the spectrum of the micro-mortar, because all other reference compounds had an oscillation amplitude minimum at this k value. Other possible Fe-bearing phases present in the micro-mortar may be C-(F)-S-H phases (Mancini et al. 2020), whereas hematite and goethite are clearly excluded. Results thus pointed to the presence of Fe in various environments in the sample, corroborating conclusions obtained by analysis of the XANES. Note that XANES and EXAFS spectroscopy both exclude the presence of detectable amounts of ferrous (Fe(II)) or elemental iron. Observed differences in Fe speciation between both compounds can only be attributed to the presence of low amounts of Fe in the aggregates. Furthermore, only octahedral ferric iron Fe(III) was detected in the concrete although in this case no clear phases could be identified.

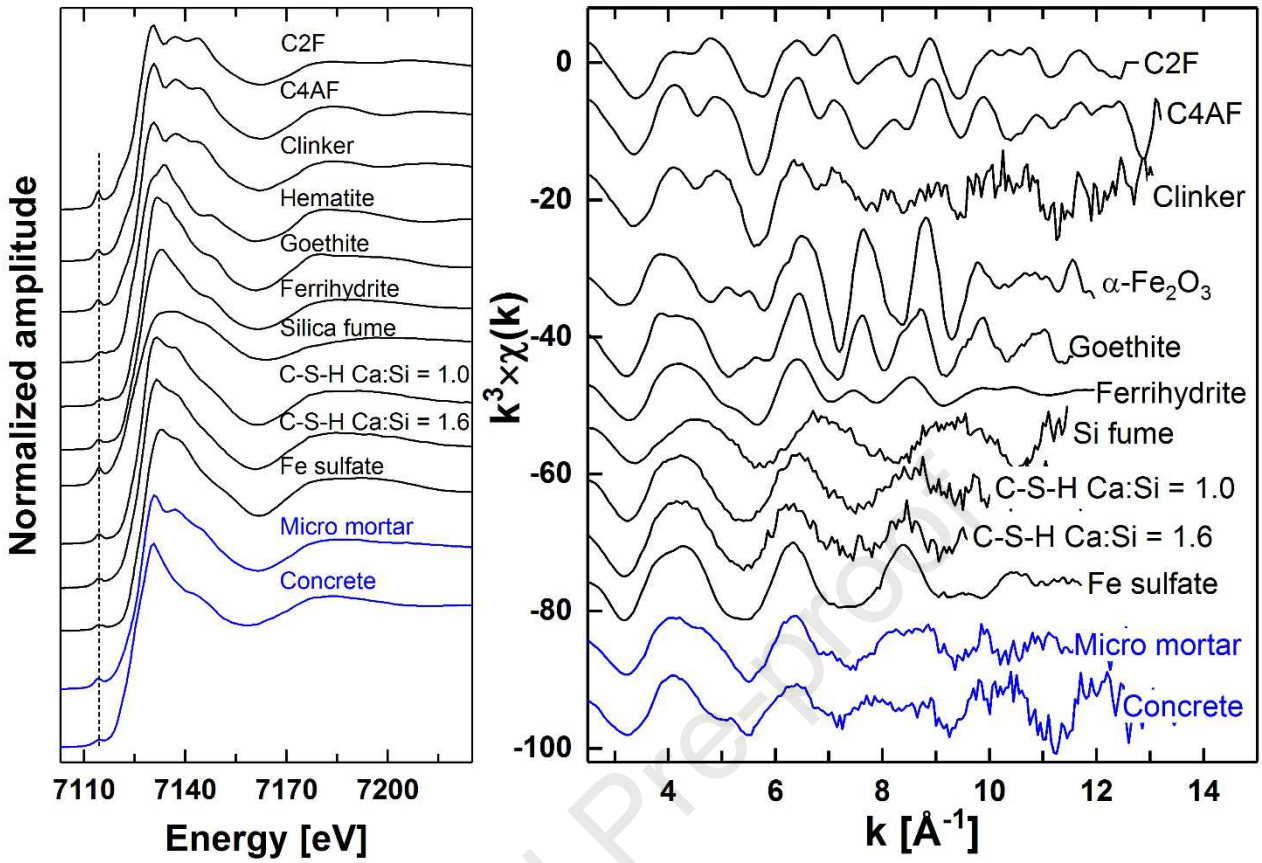

Figure 5: *Fe K-edge XANES (left) and EXAFS spectra (right) of the micro-mortar, the concrete and the reference compounds. The vertical dashed line in the XANES indicates the position of the pre-edge features.*

For chlorine, only Cl K-edge XANES were recorded for the micro-mortar, the concrete and reference compounds (Figure 6). The XANES of the liquid reference compounds differed significantly from that of all solid compounds. For the solid compounds, the maximum of the main absorption edge was located at similar energy position, implying that all compounds contained chloride ions. Friedel's and Kuzel's salt have very similar XANES with a shoulder at ~2827 eV, hinting at comparable environments. The XANES of both C-S-H phases differed: the XANES of the phase with higher Ca content had a weak shoulder at ~2827 eV, whereas the XANES of the phase with higher Si content exhibited a distinctive feature at ~2833 eV. The XANES of the sodium, calcium and potassium chloride differed from each other, in agreement with differences in their crystal structures. XANES of the micro-mortar and the concrete were very similar. This result hinted at comparable Cl environments in the samples, and excluded the presence of significant amounts of reference compounds such as C-S-H phases, Kuzel's and Friedel's salts, NaCl and KCl. The XANES of $CaCl_2.2H_2O$ bore similarities with the samples, however the absorption edge was wider and higher in amplitude. Consequently, Cl can only be bound, physically or chemically, to another mineral phase present in the samples. Additional reference compounds would be needed to identify the Cl binding environment in the micro-mortar and in the cement.

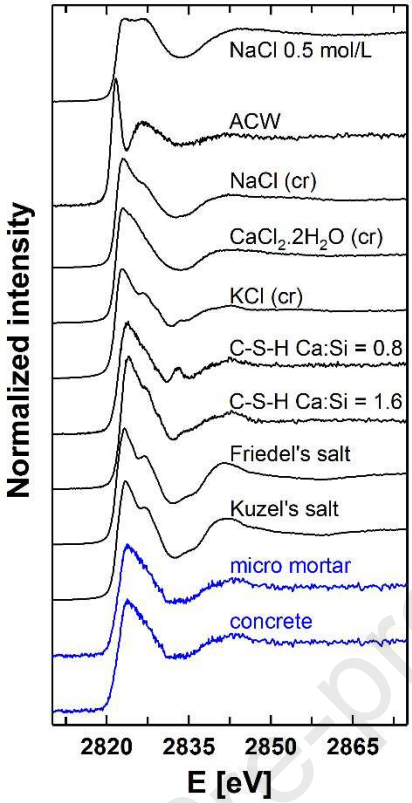

Figure 6: *Cl K-edge XANES of the micro-mortar, the cement and reference compounds.*

Table 10. Hydrates and raw materials identified (Id.) / quantified in the concrete and the micro-mortar

	Concrete	Micro-mortar
Hydration phases		
C-(A)-S-H	Id.*	Id.*
C-(F)-S-H	Not observed	Id.
Ettringite	Id. (minor)	Id. (minor)
Hydrotalcite	Not observed	Id.
Friedel´s salt	Not present	Not present
Kuzel´s salt	Not present	Not present
Bound water	Not determined	11%
Raw materials		
Alite/Belite	Not observed	Id.
Ferrites	Not observed	C2F[a] /C4AF[b]
Blast furnace slag	Id.	Id.
Quartz filler	Id.	Id.
Calcite	Not observed	< 2.0 wt. %
Silica Fume	Id.	Id.

*Ca/Si ratio =0.5-0.7 and Al/Si-ratio = 0.05

[a] Dicalcium ferrite [$Ca_2Fe_2O_5$]

[b] Tetracalcium alumino ferrit [Ca_2FeAlO_5]

4.5 Percolation experiments with concrete

Percolation experiments were performed with the concrete and using two different water compositions, Granitic II and Clay II, representing the dilute Grimsel groundwater (pH = 9.7) and the FEBEX bentonite

porewater (pH = 8.0), respectively. Table 11 shows that the evolution of the pH (within 1 cm depth) as a function of time is kept approximately constant during 660 days and with values similar to the pH of the water injected. This observation indicates that at the high pressure of the injected water, chemical equilibrium with the cement hydrates has not been produced. Very low hydraulic conductivities of $1x10^{-13}$ m/s were also obtained with the same percolation experiments as a function of time and independently of the water used. This low value is in agreement with the low porosity measured for this material (see Table 7). It was also observed that only at exposure times > 600 days the hydraulic conductivity diminishes to $1x10^{-14}$ m/s probably indicating decreasing of porosity due to precipitation reactions.

Regarding the chemical composition of the cement paste of the concrete after > 600 days of exposure to both waters indicates a clear change in the CaO/SiO_2 -ratio that occurs similarly with both waters. In addition a clear increase in Mg was observed in the sample exposed to the Clay II water. The formation of a calcite layer (<10µm) on the surface in contact with the water is also detected in all cases, although a less homogenous distribution was observed when using the clay water, similarly as observed by Garcia-Calvo et al. (2010) .

Table 11. *pH development of studied concrete and the micro-mortar in various temperatures, groundwater exposures and measurement set-ups. Values in brackets indicate the volume of percolated water.*

Temp.	20°C	20°C	20°C	20°C	20°C	20°C	10°C	95°C	95°C
Solution	Granitic I	Granitic II	Clay I	Clay II	Saline	Bentonite	Granitic III	Granitic III	B75
Method	Leaching	Percolation	Leaching	Percolation	Leaching	Leaching	Leaching	Leaching	Leaching
Sample	Micro-mortar	Concrete	Micro-mortar	Concrete	Micro-mortar	Micro-mortar	Micro-mortar	Micro-mortar	Micro-mortar
Time (days)	pH								
29	11.33		10.67		11.02				
30	11.42		10.89		11.15				
31	11.47		11.11		11.24				
32	11.35		11.05		11.14				
33	11.44		11.13		11.2				
37	11.37		11.21		11.29				
45							12.31		
58	11.13		10.93		10.87				
88	10.81		10.54		10.66				
120	10.64		10.48		10.74				
155	10.46		10.23		10.56				
175							11.96	11.02	
180	10.39		10.21		10.51	10.07 **			
210									
211	10.38		10.24		10.39				
265	10.52		10.17		10.55				
322							11.87	10.8	10.85
329	10.68		10.14		10.64				
330									
394	10.73	9.3* (17 ml)	10.25	8.2* (51 ml)	10.47				
450									
455							11.75	11.57	

480		9.2* (8 ml)		8.2* (56 ml)					
540									
567							11.48	10.8	10.67
660		8.9* (7 ml)		8.2* (25 ml)					

Within 1cm depth. **water composition (mg/L): Si (12.2), Mg (1.4), Na (3832), K (167), Ca (412), Cl (627), SO4 (8783), Al (1.46)

4.6 Leaching experiments with the micro-mortar

Leaching experiments at ambient temperature (20°C) were performed with the micro-mortar and using four different water compositions given in Table 3 (Granitic I, Clay I (Callovo-Oxfordian), Saline (granitic) and Bentonite (MX-80)). Although the experimental setup used with the bentonite was slightly different, similar evolution of water pH as a function of time was observed (Table 11). The pH of all the waters increased to pH ~ 10.1 - 10.5 after 180 days of reaction due to the leaching and dissolution of the micro-mortar in the aqueous solution. No apparent changes of pH were observed at longer times of interaction. In the case of the experiments performed with bentonite the chemical composition of the bentonite solution after 6 months of exposure was also measured (see Table 11). These results clearly show notable changes of cation concentration in the aqueous solution, especially for Mg and Al. Specifically, Mg concentration decreased and Al, although present in very low concentrations, increased two orders of magnitude. Other significant changes were related to the increase and decrease of one order of magnitude of the sulphate and chloride concentration, respectively. In minor degree, silicon concentration increased possible indicating dissolution of C-(A)-S-H phases.

In order to have a deeper understanding of the processes happening, post-morten analysis by SEM-EDX of the micro-mortar in contact with the different waters was also done. In addition, in order to help to identify the chemical processes occurring in that area, the cross section of the sample used with bentonite was analysed (homogenised 700 µm) giving the elemental depth profile depicted in Figure 7 (right). Hollow shell pores having sizes in the range of about 1-15 µm were identified. These pores were embedded in cement gel and appeared to be connected to the continuous capillary pore system by much smaller gel pores. From the images it can be clearly seen that the sample had an initial heterogeneous mineralogical composition. (in the studied spatial scale), identifying calcium-(aluminate)-silicate-hydrate phases, blast furnace slag, quartz filler and initial clinker (belite, ferrite) by using the false colour technique..

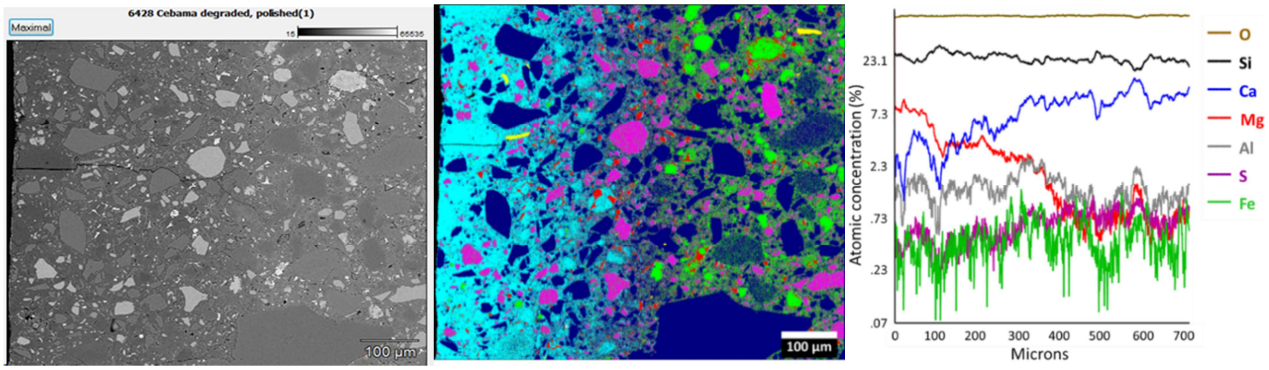

Figure 7: *Cross-section of micro-mortar after contact with bentonite pore water by SEM-EDX. Phase distributions in false colours (centre) overlaying the backscattered electron image presenting a material contrast of micro-mortar (left). Left side at images: surface of cement. Mg-exchanged C-S-H (cyan, C/S=0.17), quartz filler (blue), $MgAlCa_4Si_3O_xH_y$ (pink), belite (green), tetracalcium aluminoferrite (red),*

muscovite (yellow). Note that the crack observed in the figure was produced during the cutting of the sample after the degradation experiments. Elemental depth profile extracted from SEM-EDX map data (right).

Although, contact time with the four waters was different, similar processes were identified in all cases and explained in the following. A clear reaction front was observed in the micro-mortar in contact with the four waters (Figures 7 and 8). In the case of the experiment performed with bentonite (180 contact days), the reacting front was 400 µm from the surface. In all the cases, calcium content was depleted in this area compared to non-affected internal parts of the samples. In groundwater compositions containing substantial magnesium concentrations (Clay I and Bentonite), a magnesium enrichment was observed in the reaction front (Figure 7 and Figure 8). This process is mainly occurring due to the high gradient in Mg concentration between (the bentonite and Clay I) waters and the cement solid. Magnesium diffused into the solid sample and accumulated at the interface, probably sorbing on silicate structures or precipitating as new Mg structures (Bernhard et al. 2018b). As recently described in the literature (Dauzeres et al. 2016, Bernard et al. 2018a, 2020a, González-Santamaria et al. 2020), this magnesium enrichment starts with the pH decrease and chemical destabilization of the C-S-H phases and their partial decalcification and release of calcium. Due to the Ca:Si decrease, more amorphous silica structure are present which possibly favours the formation of M-S-H phases (Bernard et al. 2017) which clearly have different chemical structure than C-S-H phases (Roosz et al. 2015, 2016, Bernhard et al., 2019a, 2019b, 2020b). However, the nature and the structure of the magnesium bearing phases in the enriched zone could not be elucidated by the experimental techniques used in this work. In the case of the bentonite experiment, magnesium concentration close to the surface was three times higher than calcium suggesting the formation of magnesium-silicate-hydrate phases by decalcification of the C-S-H phases. This would agree with the observed decreasing atomic ratio with the distance. At 140 µm the Mg/Ca -ratios were equal and at 400 µm the Ca/Mg-ratio kept constant and equal to the initial ratio, suggesting that the reactive front during 6 months was 400 µm. This observed processes were similar to the ones described in Mäder et al. (2017) when describing the interface between a low-pH concrete and Opalinus clay in an in-situ experiment.

Other cation exchange with calcium, observed when using Bentonite water, was Na, which was present initially in high concentration in the water (~ 0.25M) and decreased after 6 month interaction. In addition, the elemental depth profile showed a decrease of sulphate in the altered zone in agreement with the increase of sulphate in the bentonite water. Apart from these main processes, it seems also obvious that the clinker (belite and ferrite) was hydrating/reacting in the magnesium exchanged zone with the aqueous solution to form magnesium containing phases (i.e. M-S-H phases). It can be seen that the blast furnace slag and the quartz filler remained in the samples as non-reactive solids or presenting a slow kinetic dissolution.

Precipitation of calcite and gypsum had only been observed on the holes present in the surface in contact with the bentonite water and not in the pore structure. The formation of a solid containing calcium was also observed at the surface of the solid sample, when the saline groundwater was used. It is likely that the formation of these solid in the surface decreased the rate of magnesium penetration into the micro-mortar, as a difference between clay- and saline groundwater was observed.

Finally leaching experiments at different temperatures (10°C and 95°C) with the Granitic III and bentonite B75 water were performed. Differences on the measured pH at different temperatures, but using the same Granitic III water, was observed, most probably due to the influence of temperature on the pH values. On the other hand pH values obtained at 95°C with both, granitic and B75 waters gave very similar values, indicating that similar reactions are occurring with both waters at this temperature. For micro-mortar

samples in direct contact with bentonite slurry (B75) at both temperatures, a calcium enrichment (precipitation) was observed in the surface (Figure 9) being more pronounced at 95°C within the studied timescales (567 days). Other major changes were not identified when using the Granitic III water at 10°C.

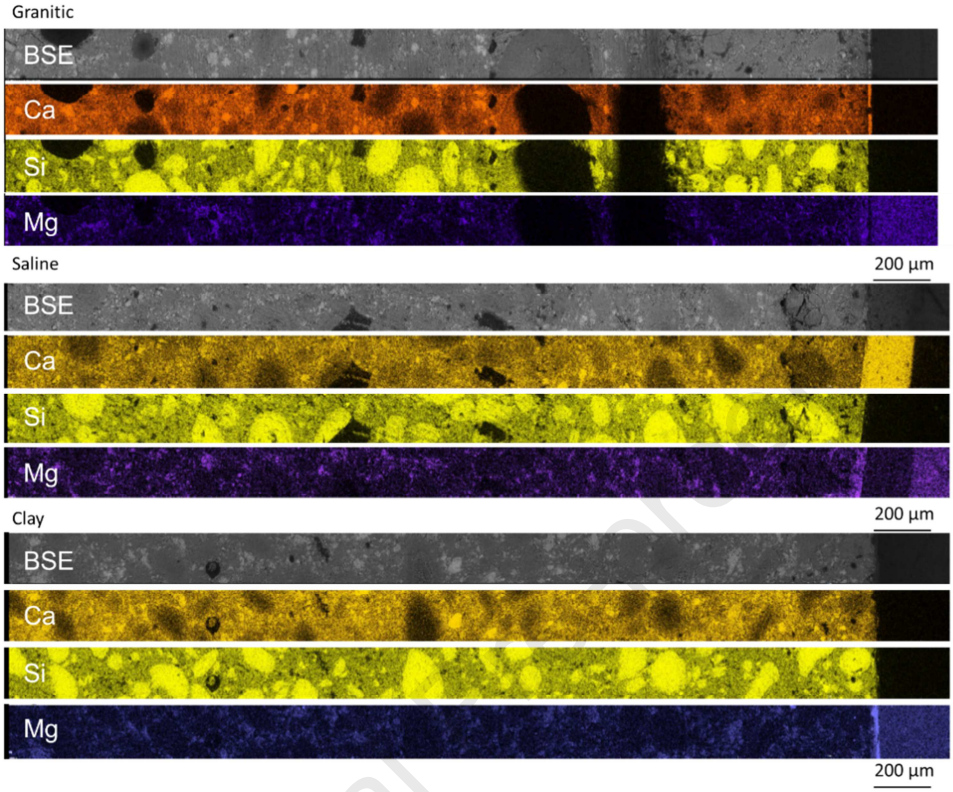

Figure 8: *Scanning elemental maps of Ca, Si and Mg in micro-mortars exposed to Granitic I, Saline and Clay I -groundwater.*

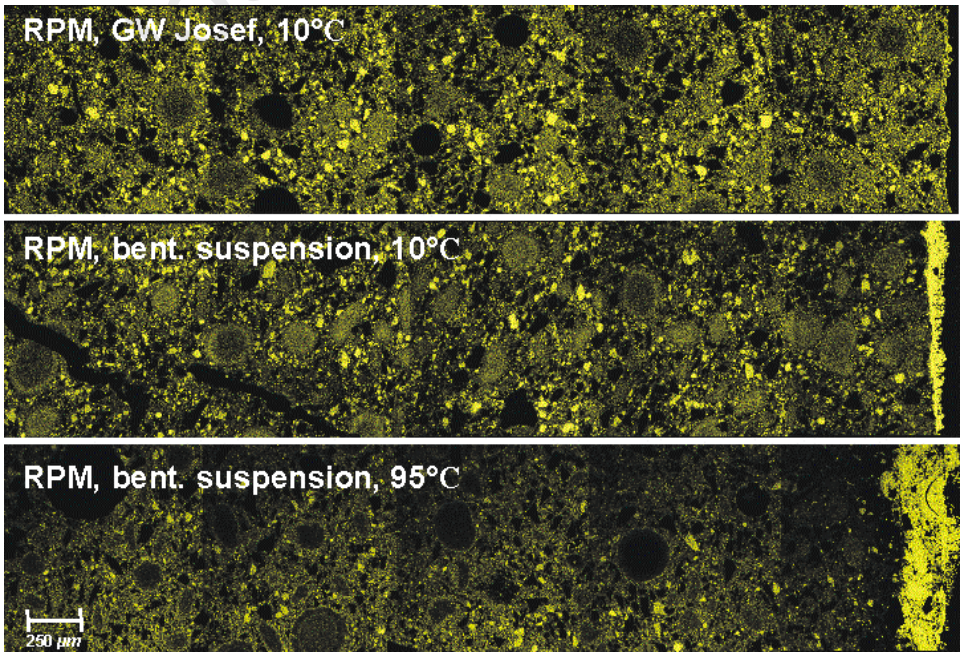

Figure 9: *Scanning electron images with Ca elemental map (yellow) showing the calcium enrichment at the interaction boundary with Granitic III (top), bentonite suspension (water B75) at 10 (middle) and 95°C (bottom).*

5. CONCLUSIONS

A new designed slag-based "low-pH" concrete and micro-mortar have been manufactured and characterized within the Cebama project in order to be used as a reference material in different experiments and modelling work. Several experimental techniques available in different laboratories around Europe have provided mechanical, hydraulic and geochemical properties of these new materials as a function of time. Compressive strengths, pore solution pH and pH development were comparable to fly ash and silica fume based "low-pH" mix designs on the basis of literature.

The compressive strengths of the concrete and micro-mortar were very high and comparable to high performance concretes. Microstructural analyses showed dense and homogeneous microstructures with low porosity mainly in the nanoscale range providing very low hydraulic conductivities. Chemical characterisation of the micro-mortar identified C-S-H and C-(A)-S-H phases as the main hydrates. Ca/Si ratio were between 0.5-0.7 and Al/Si-ratio around 0.05 for these solid phases. Minor phases were ettringite and hydrotalcite and the pore solution pH was below the saturation pH of portlandite, in agreement with the solid characterization and other "low-pH" formulations described in the literature. XAS analysis provided information on Fe and Cl speciation for the first time in this kind of low-pH cementitious materials. The data suggest that the Fe environment in the micro-mortar differed from that in the concrete, and that Fe was present only as ferric iron in both materials. In the micro-mortar, Fe was present at both tetrahedral and octahedral sites. Binding environments may be similar to that in C2F or C4AF, and possibly C-(F)-S-H phases. In the concrete, data suggest that Fe predominated at octahedral sites. Upcoming modelling of EXAFS data will provide additional information in terms of the nature and numbers of neighbouring atoms and bond distances. On the other hand, XAS pointed to a similar binding environment for Cl in the micro-mortar and cement, and ruled out the presence of Cl in an environment comparable to that in the liquid phase. Data also excluded the presence of Cl in an environment comparable to that in Kuzel's or Friedel's Salt and Cl incorporated in C-S-H phases. The use of additional reference compounds would be needed to obtain information on Cl speciation.

Alteration of the micro-mortar in contact with different representative pore- and groundwaters in nuclear waste disposal, was observed within relatively short exposure times compared to the lifetime of a repository. However, should be kept in mind that high solid/liquid ratios were used to accelerate the laboratory leaching experiments that are not representative of real repository scenarios. In all the cases, calcium content was depleted in the alteration zone of the solid compared to non-affected internal parts of the samples. Micro-mortar in contact with magnesium containing porewaters, specifically with clay and bentonite waters, at 20°C, shows a Mg enrichment through the solid, due to a significant chemical gradient between both materials. Possible precipitation of Mg phases, such M-S-H phases with complex chemical structures or brucite occurred in this zone. This was not observed when granitic waters was used. Calcium depletion and magnesium enrichment at the reaction front is not a unique quality of slag-based "low-pH" mix designs. Similar reaction front has been observed also in fly ash and silica fume based "low-pH" mix designs in contact with clays in field and laboratory experiments.

All these results clearly show that the performance of "low-pH" mix designs of this work exceeds the performance of traditional Portland cement concretes and are comparable to high performance concretes. "Low-pH" mix designs are thus very suitable construction materials, if the mix design is performed accordingly and the mixing methodology and emplacement method results in a homogeneous mix. In

addition, it can be deduced that slag is able to replace fly ash when producing ternary ”low-pH” mixtures in the future, if needed due to material supply or quality problems. Other interesting results are related to the use of XAS techniques to identify minor phases in cementitious systems.

ACKNOWLEDGEMENTS

The research leading to these results has received funding from the European Union's European Atomic Energy Community's (Euratom) Horizon 2020 Programme (NFRP-2014/2015) under grant agreement, 662147 - “Cebama”. V. Montoya acknowledge the German Federal Ministry of Education and Research (Grant 02NUK053A) and the Initiative and Networking Fund of the Helmholtz Association (Grant SO-093) within the iCross project for partial funding. Additionally, KIT-INE acknowledges the ESRF and the KIT Synchrotron Light Source for provision of synchrotron radiation beam time and D. Banerjee for assistance during measurements at the BM26A beamline. We thank B. Lothenbach (EMPA, Switzerland) and S. Grangeon (BRGM, France) for providing reference compounds for the XAS study. The authors also acknowledge the support provided by many supervisors and technical experts during the course of this work: Dieter Schild, Thorsten Schäfer, Christian Adam, Kathy Dardenne and Jörg Rothe from KIT; A. Fernandez and J.L. Garcia-Calvo from CSIC; M. Felipe-Sotelo and M. Isaacs from University of Surrey; Tomáš Rosendorf from ÚJV Řež, a. s.; John Provis and Neil Hyatt from University of Sheffield; Mia Löija and Hanna Litti from VTT and four anonymous reviewers for their careful reading of the paper and their many insightful comments and suggestions.

REFERENCES

Alonso, M.C., Garcia Calvo, J.L., Walker, C., 2012. Development of an accurate pH measurement methodology for the pore fluids of low pH cementitious materials. SKB report R-12-02, Sweden.

ANDRA (2005) Argile, synthesis evaluation of the feasibility of a geological disposal in an argillaceous formation (2005) https://international.andra.fr/ (accessed 17.07.20)

Bach, T.T.H., 2010. Physico-chemical evolution of low-pH cements : influence of the temperature and the retention mechanisme of alkalins. Thesis, Université de Bourgogne.

Bernard, E. 2017a. Magnesium silicate hydrate (M-S-H) characterization: temperature, calcium, aluminum and alkali. Thesis. Université Bourgogne Franche-Comté. France

Bernard, E., Dauzères A., Lothenbach, B, 2018b. Magnesium and calcium silicate hydrates, Part II: Mg-exchange at the interface “low-pH” cement and magnesium environment studied in a C-S-H and M-S-H model system, Applied Geochemistry, 89, 210-218

Bernard, E., Jenni, A., Fisch, M., Grolimund, D., Mäder U. 2020a. Micro-X-ray diffraction and chemical mapping of aged interfaces between cement pastes and Opalinus Clay. Applied geochemistry, 104538

Bernard, E, Lothenbach, B., Cau-Dit-Coumes, C., Chlique, C., Dauzeres, A., Pochard, I. 2018a.Magnesium and calcium silicate hydrates, Part I: Investigation of the possible magnesium incorporation in calcium silicate hydrate (CSH) and of the calcium in magnesium. Applied Geochemistry 89, 229-242

Bernard, E., Lothenbach, B., Chlique, C., Wyrzykowski, M., Dauzeres, A., Pochard, I., Cau Dit-Coumes. 2019b. Characterization of magnesium silicate hydrate (MSH).Cement and concrete research 116, 309-330

Bernard, E., Lothenbach, B., Le Goff, F. Pochard, I., Dauzères A. 2017c. Effect of magnesium on calcium silicate hydrate (CSH) Cement and Concrete Research 97, 61-72

Bernard, E. Lothenbach, B., Rentsch, D., Pochard, I., Dauzères A., 2017b Formation of magnesium silicate hydrates (MSH) Physics and Chemistry of the Earth, Parts A/B/C 99, 142-157

Bernard, E., Lothenbach, B., Cau-Dit-Coumes, C., Pochard, I., Rentsch D. 2020b. Aluminum incorporation into magnesium silicate hydrate (MSH) Cement and concrete research 128, 105931

Bernard, E., Lothenbach, B., Pochard, I., Cau-Dit-Coumes C. 2019a. Alkali binding by magnesium silicate hydrates Journal of the American Ceramic Society 102 (10), 6322-6336

Borghel-Bouny, V., Andrade, C., Torrent, R., Scrivener, K., 2007. Durability indicators: relevant tools for performance-based evaluation and multi-level prediction of RC durability, in Baroghel et al. Proceedings : International RILEM Workshop on Performance Based Evaluation and Indicators for Concrete Durability , pro047

Bradbury, M.H., Baeyens, B., 2011. Physico-chemical characterisation data and sorption measurements of Cs, Ni, Eu, Th, U, Cl, I and Se on MX-80 bentonite. PSI report 11-05, Switzerland.

Bruno, J., Montoya, V., 2012. From aqueous solution to solid solutions: A process oriented review of the work performed within the FUNMIG project. Appl. Geochemistry 27, 444–452. https://doi.org/10.1016/J.APGEOCHEM.2011.09.013

Cau Dit Coumes, C., Courtois, S., Nectoux, D., Leclercq, S., Bourbon, X., 2006. Formulating a low-alkalinity, high-resistance and low-heat concrete for radioactive waste repositories. Cem. Concr. Res. 36, 2152–2163. https://doi.org/10.1016/j.cemconres.2006.10.005

Codina, M., Cau-dit-Coumes, C., Le Bescop, P., Verdier, J., Ollivier, J.P., 2008. Design and characterization of low-heat and low-alkalinity cements. Cem. Concr. Res. 38, 437–448. https://doi.org/10.1016/J.CEMCONRES.2007.12.002

Colville, A.A., Geller, S., 1971. The crystal structure of brownmillerite, Ca${\sb 2}$FeAlO${\sb 5}$. Acta Crystallogr. Sect. B 27, 2311–2315. https://doi.org/10.1107/S056774087100579X

Czech Geological Institute, 1987. Metodiky laboratorních zkoušek v mechanice zemin a hornin (Methods of laboratory testing in soil and rock mechanics). Prague.

Dauzeres, A., Achiedo, G., Nied, D., Bernard, E., Alahrache, A., Lothenbach B. 2016. Magnesium perturbation in low-pH concretes placed in clayey environment—solid characterizations and modeling Cement and Concrete Research 79, 137-150

Dauzères, A., Le Bescop, P., Cau-Dit-Coumes, C., Brunet, F., Bourbon, X., Timonen, J., Voutilainen, M., Chomat, L., Sardini, P., 2014. On the physico-chemical evolution of low-pH and CEM I cement pastes interacting with Callovo-Oxfordian pore water under its in situ CO2 partial pressure. Cem. Concr. Res. 58, 76–88. https://doi.org/10.1016/J.CEMCONRES.2014.01.010

Dilnesa, B.Z., Wieland, E., Lothenbach, B., Dähn, R., Scrivener, K.L., 2014. Fe-containing phases in hydrated cements. Cem. Concr. Res. 58, 45–55. https://doi.org/10.1016/J.CEMCONRES.2013.12.012

Dole, L.R., Mattus, C.H., 2007. Low pH concrete for use in the US high-level waste repository: Part I overview, in: Proceeding 2nd Workshop R&D on Low PH Cement for a Geological Repository, Madrid, Spain, June. pp. 15–16.

Engelhardt, G., Michel, D., 1987. High-resolution solid-state NMR of silicates and zeolites. John Wiley and Sons,New York, NY, United States.

Finck, N., Schlegel, M.L., Dardenne, K., Adam, C., Kraft, S., Bauer, A., Robert, J.-L., 2019. Structural iron in smectites with different charge locations. Phys. Chem. Miner. 46, 639–661. https://doi.org/10.1007/s00269-019-01028-y

Gaboreau, S., Prêt, D., Tinseau, E., Claret, F., Pellegrini, D., Stammose, D., 2011. 15 years of in situ cement–argillite interaction from Tournemire URL: Characterisation of the multi-scale spatial heterogeneities of pore space evolution. Appl. Geochemistry 26, 2159–2171.

802 https://doi.org/https://doi.org/10.1016/j.apgeochem.2011.07.013

803 Gallé, C., 2001. Effect of drying on cement-based materials pore structure as identified by mercury
804 intrusion porosimetry: A comparative study between oven-, vacuum-, and freeze-drying. Cem. Concr.
805 Res. 31, 1467–1477. https://doi.org/10.1016/S0008-8846(01)00594-4

806 Garcia-Calvo, J.L., Hidalgo, A., Alonso, C., Fernandez Luco, L., 2010. Development of low-pH cementitious
807 materials for HLRW repositories. Resistance against ground waters aggression. Cem. Concr. Res. 40,
808 1290–1297. https://doi.org/10.1016/j.cemconres.2009.11.008

809 Garcia, J.L., Alonso, M.C., Hidalgo, A., Luco, L., Fernández, 2007. Design of low-pH cementitious materials
810 based on functional requirements, in: Proceedings R&D on Low-PH Cement for a Geological
811 Repository, 3rd Workshop, June. pp. 13–14.

812 Gascoyne, M., 2002. Influence of grout and cement on groundwater composition. Working Report 2002-07,
813 POSIVA, Finland

814 González-Santamaría D.E., Fernández R., Ruiz A.I., Ortega A., Cuevas J 2020 . High-pH/low pH ordinary
815 Portland cement mortars impacts on compacted bentonite surfaces: Application to clay barriers
816 performance. Applied Clay Science, 193, 105672

817 Holt, E., Claret, F., Mäder, U., 2016. Report on WP1 selected experimental materials to be used, including
818 both new laboratory and aged in-situ samples. CEBAMA Deliverable D1.05.

819 Holt, E., Koho, P., 2016. POPLU Experimental summary report. DOPAS project, Deliverable D4.5.

820 Holt, E., Leivo, M., Vehmas, T., 2014. Low-pH concrete developed for tunnel end plugs used in nuclear
821 waste containment, in: Concrete Innovation Conference (CIC2014). 11 - 13 June 2014, Oslo.

822 Idiart, A., Lavina, M., Kosakowski, G., Cochepin, B., Meeussen, J., Samper, J., Mon, A., Montoya, V., Munier,
823 J., Poonoosami, J., Montenegro, L., Deissman, G., Rohmen, S., Hax Damiani, L., Coene, E., Nieves, A.,
824 2020. Reactive transport modelling of a low-pH concrete / clay interface. Appl. Geochemistry, 115,
825 104562

826 Koskinen, K., 2014. Effects of Cementitious Leachates on the EBS. Posiva Oy 31.

827 L'Hôpital, E., Lothenbach, B., Kulik, D.A., Scrivener, K., 2016. Influence of calcium to silica ratio on
828 aluminium uptake in calcium silicate hydrate. Cem. Concr. Res. 85, 111–121.
829 https://doi.org/10.1016/J.CEMCONRES.2016.01.014

830 Lagerblad, B., Trägårdh, J., 1994. Conceptual model for concrete long time gradation in a deep nuclear
831 waste repository. SKB Technical report, 95-21, Sweden

832 Leivo, M., Vehmas, T., Holt, E., 2014. Developing Low pH concrete for tunnel plugging structures in nuclear
833 waste containment, in: XIII Nordic Concrete Research Symposium - Reykjavik, Iceland Duration: 13
834 Aug 2014 → 15 Aug 2014. pp. 491–494.

835 Leroy, P., Hördt, A., Gaboreau, S., Zimmermann, E., Claret, F., Bücker, M., Stebner, H., Huisman, J.A., 2019.
836 Spectral induced polarization of low-pH cement and concrete. Cem. Concr. Compos. 104, 103397.
837 https://doi.org/10.1016/J.CEMCONCOMP.2019.103397

838 Lothenbach, B., Le Saout, G., Ben Haha, M., Figi, R., Wieland, E., 2012a. Hydration of a low-alkali CEM III/B–
839 SiO2 cement (LAC). Cem. Concr. Res. 42, 410–423.
840 https://doi.org/10.1016/J.CEMCONRES.2011.11.008

841 Lothenbach, B., Wieland, E., Schwyn, B., Figi, R., Rentsch, D., 2008. Hydration of low-pH cements., in:
842 International Workshop on the Mechanisms and Modelling of Cement / Waste Interactions,. *Le*
843 *Croisic, France,*

Mäder, U., Jenni, A., Lerouge C., Gaboreau, S., Miyoshi, S., Kimura, Y, Cloet, V., Fukaya, M., Claret, F., Otake, T, Shibata M., Lothenbach B. (2017). 5-year chemico-physical evolution of concrete–claystone interfaces, Mont Terri rock laboratory (Switzerland). Swiss J. Geosci. 110, 307.

Mancini, A., Wieland, E., Geng, G., Dähn, R., Skibsted, J., Wehrli, B. Lothenbach B (2020) Fe (III) uptake by calcium silicate hydrates. Applied Geochemistry, 113, 104460

Martino, J.B., 2007. Low heat high performance concrete used in a full-scale tunnel seal, in: Proceeding 3rd Workshop R&D on Low PH Cement for a Geological Repository, Paris, June. pp. 13–14.

Moren, L., 2010. Design and production of the KBS-3 repository, Technical. Report TR-10-12 ed. Svenskt Kärnbränslehantering AB.

Nagra,2019 n.d. Timetable [WWW Document]. Nagra. URL https://www.nagra.ch/en/timetable.htm# (accessed 6.28.19).

Nikitenko, S., Beale, A.M., van der Eerden, A.M.J., Jacques, S.D.M., Leynaud, O., O'Brien, M.G., Detollenaere, D., Kaptein, R., Weckhuysen, B.M., Bras, W., 2008. Implementation of a combined SAXS/WAXS/QEXAFS set-up for time-resolved {\it in situ} experiments. J. Synchrotron Radiat. 15, 632–640. https://doi.org/10.1107/S0909049508023327

Nishiuchi, T., Yamamoto, T., Hironaga, M., Ueda, H., 2007. Mechanical properties of low pH concretes, LAC, HFSC AND SAC, in: Proceeding 3rd Workshop R&D on Low PH Cement for a Geological Repository, Paris, June. pp. 13–14.

Noiret, A., Bethmont, S., Bosgiraud, J., Foin, R., 2012. DOPAS Work Package 4 Deliverable 4.8FSS Experiment Summary Report.

Palomäki, J., Ristimäki, L., 2013. Facility Description 2012: Summary Report of the Encapsulation Plant and Disposal Facility Designs, Working Report 2012-66.

Posiva Oy, 2020 n.d. General Time Schedule for Final Disposal [WWW Document]. Posiva Oy Olkiluoto, 27160 Eurajoki. http://www.posiva.fi/en/final_disposal/general_time_schedule_for_final_disposal#.XorbmEASs2w. (accessed 06.04.20).

Proux, O., Nassif, V., Prat, A., Ulrich, O., Lahera, E., Biquard, X., Menthonnex, J.-J., Hazemann, J.-L., 2006. Feedback system of a liquid-nitrogen-cooled double-crystal monochromator: design and performances. J. Synchrotron Radiat. 13, 59–68. https://doi.org/10.1107/S0909049505037441

Ravel, B., Newville, M., 2005. Data analysis for X-ray absorption spectroscopy using IFEFFIT. J. Synchrotron Radiat. 12, 537–541. https://doi.org/10.1107/S0909049505012719

Richardson, I.., 1999. The nature of C-S-H in hardened cements. Cem. Concr. Res. 29, 1131–1147. https://doi.org/10.1016/S0008-8846(99)00168-4

Rothe, J., Butorin, S., Dardenne, K., Denecke, M.A., Kienzler, B., Löble, M., Metz, V., Seibert, A., Steppert, M., Vitova, T., Walther, C., Geckeis, H., 2012. The INE-Beamline for actinide science at ANKA. Rev. Sci. Instrum. 83, 043105. https://doi.org/10.1063/1.3700813

Roosz, C. 2016. Thermodynamic properties of hydrated cement phases: C-S-H, C-A-S-H and M-S-H. Thesis, Universite de Poitiers, France

Roosz, C., Grangeon, S., Blanc, P., Montouillout, V., Lothenbach, B., Henocq, P., Giffaut E., Vieillard, P., Gaboreau, S. 2015 Crystal structure of magnesium silicate hydrates (MSH): The relation with 2: 1 Mg–Si phyllosilicates. Cement and Concrete Research 73, 228-237

Roosz, C., Vieillard, P., Blan, P., Gaboreau, S., Gailhanou, H., Braithwaite, D., Montouillout, V., Denoyel, R.,

Henocq, P., Madé, B. Thermodynamic properties of C-S-H, C-A-S-H and M-S-H phases. 2018. Results from direct measurements and predictive modelling. Applied Geochemistry, 92, 140-156

Schöler, A., Lothenbach, B., Winnefeld, F., Zajac, M., 2015. Hydration of quaternary Portland cement blends containing blast-furnace slag, siliceous fly ash and limestone powder. Cement Concrete Composite 55, 374–382.

Scrivener, K., Snellings, R., Lothenbach, B., 2018. A practical guide to microstructural analysis of cementitious materials. Crc Press. Taylor and Francis Group

Taylor, H.F.W., 1997. Cement Chemistry, 2nd ed. Thomas Telford Publishing, Thomas Telford Services Ltd, London.

Turrero, M., Fernández, A., Peña, F., SÁNCHEZ, M.D., Wersin, P., Bossart, P., Sánchez, M., MELÓN, A., Garralón, A., de Llano, A., Gómez, P., HERNÁN, P., 2006. Pore water chemistry of a Paleogene continental mudrock in Spain and a Jurassic marine mudrock in Switzerland: Sampling methods and geochemical interpretation. J. Iber. Geol. 2006.

Turrero, M., Villar, M., Torres, E., Escribano, A., Cuevas, J., Fernandez, R., Ruiz, A., Vigil de la Villa, R., Soto, I., 2011. Laboratory tests at the interfaces: first results on dismantling of tests FB3 and HB4. PEBS Proj. Deliv. D2.3-3-1.

Vasconcelos, R. Walkley, B., Day, S. Tang C., Paraskevoulakos H., Gardner L, Corkhill C. (2020) 18-month hydration of a low-pH cement for geological disposal of radioactive waste: The Cebama reference cement, Applied Geochemistry, in print

Vašíček, R., Červinka, R., P, V., T, R., J, S., 2018. Geochemical and Thermal Impacts on the Characteristics of Cementitious Materials: Strength, Leachate pH, Mineralogy And Diffusion, in: Third Annual Workshop of the HORIZON 2020 CEBAMA Project. Nantes.

Vašiček, R., Večernik, P., Hloušek, J., Červinka, R., Hausmannová, L., Havlová, V., 2019. Interaction between cement and Czech bentonite under temperature load and in in-situ conditions: results after first testing period, in Altmaier et al. : Proceedings of the Second Workshop of the HORIZON 2020 CEBAMA Project. KIT Scientific Reports; 7752. p. 93.

Večernik, P., Hausmannová, L., Cervinka, R., Vašiček, R., Roll, M., Hloušek, J., Havlová, V., 2016. Interaction between cement and Czech bentonite under temperature load and in in-situ conditions: an overview of experimental program. In Altmaier et al. 1st Annual workshop cebama proceedings cebama Proc. KIT Scientific report 7734, 77, Germany.

Vehmas, T., Schnidler, A., Löija, M., Leivo, M., Holt, E., 2017. Reference mix design and castings for low-pH concrete for nuclear waste repositories. Horiz. 2020 CEBAMA Proj. 101.

Vespa M., E. Wieland, R. Dähn, B. Lothenbach (2015) Identification of the thermodynamically stable Fe-containing phase in aged cement pastes. J. Am. Ceram. Soc. 98, 2286

Vinsot, A., Mettler, S., Wechner, S., 2008. In situ characterization of the Callovo-Oxfordian pore water composition. Phys. Chem. Earth, Parts A/B/C 33, S75–S86. https://doi.org/10.1016/J.PCE.2008.10.048

Walkley B, Provis J.L. 2019 Solid-state nuclear magnetic resonance spectroscopy of cements. Materials Today Advances, 1, 100007

Washburn, E.W., 1921. The dynamics of capillary flow. Phys. Rev. 17, 273.

Westre, T.E., Kennepohl, P., DeWitt, J.G., Hedman, B., Hodgson, K.O., Solomon, E.I., 1997. A Multiplet Analysis of Fe K-Edge 1s → 3d Pre-Edge Features of Iron Complexes. J. Am. Chem. Soc. 119, 6297–6314. https://doi.org/10.1021/ja964352a

928 World Nuclear Association, n.d. Radioactive waste Management [WWW Document]. URL
929 http://www.world-nuclear.org/information-library/nuclear-fuel-cycle/nuclear-wastes/radioactive-
930 waste-management.aspx (accessed 28.06.19).

931 Zhang, Z., Zhu, Y., Zhu, H., Zhang, Y., Provis, J.L., Wang, H., 2019. Effect of drying procedures on pore
932 structure and phase evolution of alkali-activated cements. Cem. Concr. Compos. 96, 194–203.
933 https://doi.org/10.1016/J.CEMCONCOMP.2018.12.003

934

- The performance of “low-pH” mix designs containing slag exceeds the performance of traditional Portland cement concretes and are comparable to high performance concretes containing fly ash and silica fume.
- That slag is able to replace fly ash when producing ternary ”low-pH” mixtures in the future, if needed due to material supply or quality problems
- Several experimental techniques (XRD, XAS at the Fe and Cl K-edges, SEM-EDX, ^{29}Si and ^{27}Al MAS NMR, TG-DSC, MIP and Kerosene porosimetry and punch strength tests) have provided mechanical, hydraulic and geochemical properties of these new designed materials.
- Micro-mortar in contact with clay and bentonite porewaters at 20°C, shows a Mg enrichment and calcium depletion at the reaction front, as similarly observed with other “low-pH” cementitious formulations in field experiments.
-

Declaration of interests

☒ The authors declare that they have no known competing financial interests or personal relationships that could have appeared to influence the work reported in this paper.

☐The authors declare the following financial interests/personal relationships which may be considered as potential competing interests: